How Mesoscale Eddies Masquerade as Rossby Waves in Newly merged Altimetric Products?

Chuanchuan Cao[1], Ge Chen[1, 2], and Xuan Wang[1*]

[1]*Department of Marine Technology, Institute for Advanced Ocean Study, Ocean University of China, China*

[2]*Qingdao National Laboratory for Marine Science and Technology, China*

[*]Corresponding author contact information:

College of Information Science and Engineering, Ocean University of China 238 Songling Road, Qingdao 266100, China

Tel: +86-532-66781265; E-mail: wangxuan_ouc@163.com

Key Points:

1) The sampling capability of six simultaneously operating altimeters is analyzed on oceanic mesoscale levels.
2) Adjacent westward propagating eddies can masquerade as long Rossby waves in Hovmöller diagram at present altimetric products.
3) The spurious wave-like and Rossby wave signals are quantified in major basins independently by re-filtering the preliminary eddies field.

Abstract

Limited by under-sampling spatiotemporal resolution of satellite altimeters, isolated and oval closed eddies can appear as wave-like patterns. This problem hindered the definitely extraction of oceanic Rossby waves in former researches. The unprecedented sampling capability of the simultaneously operating six altimeters during 2016 ~ 2019 opens an opportunity to separate Rossby waves from Mesoscale-eddies. In this paper, the sampling density of newly altimetric products is analyzed and a series of 2-dimensional finite impulse response filter is used to decompose the propagating signals. The results demonstrate that filtered wave-like patterns are mainly attribute to mesoscale-eddies and the specialized filter fail to distinguish them directly. More importantly, the spurious wave-like and real Rossby wave signals can be quantified by re-filtering the preliminary eddies field. The dominant wave signals are generally observed for biannual and annual Rossby waves in three major basins and the maximum more than 25% of observed signals in mid-latitude Pacific. The Southern Indian Ocean has the most significant annual periods signals which may implicate the role of El Niño/Southern Oscillation. In addition, the eddies can masquerade as Rossby wave within a limited latitude, which directly related to the oceanic basin, the local characteristics of eddies and the period of masqueraded waves. Based on the conservation of potential vorticity, the transient adjustment of ocean circulation to response of the large-scale atmospheric forcing from Rossby waves turn to ubiquitous vortices at increase of latitude.

Plain Language Summary

Mesoscale eddies and Planetary scale Rossby waves are two major manifestation features of ocean to response to large-scale atmospheric forcing. Eddy is an isolated and closed circulation whose streamlines are close to ovals. However, Rossby waves are composed by

several crests and troughs that approximately perpendicular to the direction of propagation of phase theoretically (Polito et al., 2015). Satellite altimetry can provide a comprehensive overview of the westward propagation features. Unfortunately, they propagate westward with approximately speed and eddies can masquerade as Rossby waves in low-resolution Altimetric data. Recently, the number of on-orbit altimeters are approximately three times than before, it provides an unprecedented chance that separate the zonally wave signals from the coherent eddies. Combining with the specialized filter and highest quality merged altimetric products and advanced eddy identification method, the results reveal that decomposed wave-like components are mainly attribute to mesoscale eddies. The spurious wave-like and real Rossby waves signals are quantified for the first time.

1 Introduction

Rossby waves own their existence to the latitudinal variation of the vertical component of the earth's vorticity, and predicted by Carl Gustave Rossby in the 1930s (Dickinson, 1978). One can determine an infinite number of Rossby wave normal modes by solving an eigenvalue problem, and they are ordered by decreasing westward phase speeds (Gill, 1982; Pedlosky, 1986). The long, first baroclinic mode Rossby waves are focused by oceanographers and induced variations of sea level anomalies (SLA) are mirrored as the vertical displacement of main thermocline which had a potentially important influence on local climate variability. The linear theory indicates that the long waves are nondispersive and transport potential energy westward that helps to maintain the mid latitude gyres and to intensify the western boundary currents (Polito and Liu, 2003). However, these waves are difficult to observe in ocean, because of their small SLA (order of 10 cm or smaller), slow propagation speed (order of 10 cm/s or less) and long wavelengths (hundreds to thousands of kilometers) (Chelton and Schlax, 1996). The

theoreticians have waited for sufficient satellite altimetric data to demonstrate the existence and nature of planetary (Rossby) waves (Killworth et al., 1997).

Thanks for the advent of satellite altimeters with such resolution, Chelton and Schlax (1996) provided the first demonstration of Rossby wave signals in world ocean with TOPEX/POSEIDON satellite altimetry. After that, these waves also find by hydrological observation in regional oceans. In the Indian ocean, Xie et al. (2002) analysis of the in-situ measurements and a model-assimilated dataset conclusion that up to 50% of the total SST variability in the western tropical South Indian Ocean is due to oceanic Rossby waves and El Niño/Southern Oscillation (ENSO) is the major forcing for these waves. Such westward-propagating thermocline-depth anomalies have been studied using in-situ/satellite measurements and ocean models and attributed to oceanic Rossby waves (*e.g.*, Perigaud and Delecluse, 1993; Masumoto and Mayers, 1998; Chambers et al., 1999; Birol and Morrow, 2001). At the same basin, Chowdary et al. (2009) using Argo profiles reveal a pronounced up-westward propagation of subsurface warming in the southern tropical Indian Ocean, which associated with Rossby waves traveling on the sloping thermocline and forced by easterly wind anomalies. In Atlantic Ocean, Chu et al. (2007) used the Argo float tracks and temperature profiles to reconstruct a spatial structure of the mid-depth circulation and identified the perturbations as annual Rossby wave (generated by alongshore wind fluctuations and/or an equatorially forced coastal Kelvin wave) and semiannual Rossby waves (generated by a nonlinear resonance mechanism). In Pacific Ocean, Bosc and Delcroix (2008) revealed that the first baroclinic mode equatorial Rossby waves to be responsible for the anomalous meridional geostrophic transports of warm water, and pointed out the effects of wind-forcing and eastern boundary reflection processes are generating these waves. Both theory and hydrologic observation has supported the existence of

first baroclinic Rossby waves and major driven mechanisms are ENSO, wind anomaly and reflected by kelvin wave.

Meanwhile, Chelton and Schlax (1996) indicated that the standard theory for freely propagating, linear, baroclinic Rossby waves is deficient in predicting the observed phase speeds. The existing theory has met with unprecedented skepticism and it also sparked the great interest to explain this discrepancy. The background mean oceanic flows and Bottom topography variations are major reasons to directly affect the speed of Rossby waves (Killworth et al, 1997; Killworth and Blundell, 1999; Killworth and Blundell, 2003a, 2003b; Killworth, 2004). Killworth and Blundell (2003a, 2003b) developed an extended theory still diverged significantly from predicted speed poleward of about 35°. Similar to Sea Surface Height (SSH) data analysis, with the help of wide swath remote sensing sensors, many researchers have found out the near-ubiquity of apparently wave-like signals in the global Sea Surface Temperature (SST) and chlorophyll-a (chl-a) records (e.g., Cipollini et al., 1997; Hill et al., 2000; Cipollini et al., 2001; Uz et al., 2001; Quartly et al., 2003). The concurrent westward patterns hold for SST, while discrepancies become apparent in chl-a fields, it raises the possibility of other mechanisms may be responsible for the wave-like patterns (Cipollini et al., 2001, 2006; Killworth et al.,2004).

With the increase number of the altimeter satellites, the resolution of the merged two satellites is about double that of one alone (Chelton and Schlax, 2003). Chelton et al (2007; 2011a; 2011b) used these high-resolution SSH fields revealed that westward propagating features previously believed to be linear Rossby waves are actually nonlinear rotating coherent eddies. This dichotomy arises because both features westward propagation at roughly same speed that due to the latitudinal dependence of the effects of Earth's rotation, so that the coherent eddies can masquerade as Rossby waves in low-resolution SSH fields. The proposal of the

nonlinear feature seems to explain the discrepancies of phase speed, as well as supported by the westward signal patterns of the SST and chl-a.

Where are the Rossby waves in the ocean? Rossby wave is a kind of vertically fluctuation phenomenon between ocean stratification and propagate mostly in the zonal direction. Although, nonlinear of mesoscale eddies allow them to trap fluid, whereas linearly Rossby waves do not. The biomass modulation of the four basic process is same for both them (McGillicuddy, 2011). Furthermore, the horizontal and vertical advection are both exist that caused by hydrographic properties gradient (*e.g.* Quartly et al.,2003; Killworth et al., 2004; Charria et al., 2006; Bosc and Delcroix, 2008; O´Brien et al., 2013) and the meridional advection are much less than its zonal and vertical counterpart (Polito and Cornillon, 1997; Charria et al., 2006; Gutknecht et al., 2010). Therefore, SSTA and chl-a data cannot be used to distinguish eddies and Rossby waves easily. O´Brien et al (2013) found that co-propagating signals can be readily observed throughout the major ocean basins in SLA, SSTA and chl-a data sets, and the characteristics strongly suggested the signals of the first-mode baroclinic Rossby waves. However, the westward propagating eddies cannot be ruled out and tropical instability waves may be responsible for some of the observed variability in the equatorial Pacific and Atlantic. Based on a criterion of $U/c>1$ that distinguish linear and nonlinear mesoscale eddies by Chelton et al. (2017), the nonlinear parts are often regarded as mesoscale-eddies and linear parts are Rossby waves. In fact, eddy often exhibit as nonlinear feature during eddies born and dead phases, and the linear and nonlinear feature are also can appear alternately during the growth phase. The nonlinear of mesoscale eddies are mostly attribute to the smaller transport speed c, which can be effect by the variation of wind stress, shear of background flow and bottom topography et al. So, it is unreasonable to regard an isolated, closed and slow-propagating mesoscale-eddies as a Planetary Rossby wave. Polito et al.

(1997, 2003, 2015) designed a series of 2-dimensional finite impulse response band-pass (2D-FIR) filter to extract and evaluate the westward propagating components from SSH measurements, which based on the characteristic of zonal propagation. They attributed wave-like signals to Rossby waves and proposed a novel conclusion that the relatively large percentage of vortices ride on Rossby waves during their whole lifetime. According to the fact that weekly temporal resolution and poor sampling capacity of two altimeters, this great works are more proof of the coexistence of wave and eddies. It is remains worthy curiosity and doubt that whether eddies can pass through the filters and masquerade as Rossby waves like earlier studies.

To sum up, it is difficult to separate the Oceanic Rossby waves from mesoscale eddies definitely in under-sampling spatiotemporal resolution. On the aspect of geometric shape, the coherent eddies can masquerade as Rossby wave in low resolution altimetric data. On the aspect of kinematics, the Rossby wave and mesoscale-eddy westward propagating at roughly same speed on the sea surface due to the latitudinal dependence of the effects of Earth's rotation (β effect). On the aspect of dynamics modulations, both features can cause hydrologic property anomalies. At present, five or six satellite altimeters are simultaneously operating on-orbit that support an unprecedented sampling capacity. Therefore, it is time to reinvestigate the conclusion of former research and whether the newly merged SLA data can distinguish these waves and eddies definitely. The rest of the paper is organized as follows: A brief description of the merged altimeter data and the methodology of eddy identification and the processes of filtering are provided in section 2. The sampling capability of current satellite altimeter and the filtered results of 2D FIR filter in Hovmöller diagrams are analyzed and described in sections 3 and 4, respectively. In section 5, a series of evidences demonstrate that the anticipative wave-like patterns in 2D filtered results are mainly attribute to mesoscale eddies. Quantify the spurious

157 wave-like and real Rossby waves signals in section 6 and A summary with conclusions is given
158 in section 7.

159 **2 Datas and Methods**

160 2.1 Altimeter data

161 The newly delayed-time altimetric products from CMEMS (Copernicus Marine
162 Environment Monitoring Service, https://marine.copernicus.eu/) are used in this study, which
163 include the Level-3 products of alongtrack altimeters and Level-4 products for "all-sat" merged
164 data of global daily mean SLA with a grid size of (1/4) °× (1/4) °. They are packed in NetCDF-4
165 files and update to 15 October 2019. Altimeter satellite gridded SLA computed with respect to a
166 twenty-year mean and processed in the Data Unification and Altimeter Combination System
167 (DUACS). The Level-4 grid data are merged by all simultaneously orbit mission and estimate by
168 Optimal Interpolation.

169 Two altimetry satellites are required to map the ocean and monitor its movements
170 precisely at scales of 100~300 kilometers, and three satellites are needed to observe eddies and
171 mesoscale phenomenon. The resolution of sea surface height measurements is greatly enhanced
172 when the four altimetry satellites are available (https://www.aviso.altimetry.fr/en/techniques/).
173 According to the history of altimeter satellites and newly "all-sat" merged data composition
174 instruction, the phases of merged altimeter can be classified by the number of on-orbit satellites:
175 two-satellites (1993~1999), three-satellites (2000~2010), four-satellites (2011~2015), five or six-
176 satellites (2016~). So we choose the newly phases product in this article.

177 2.2 Eddy identification

178 In the present analysis, a 4-step scheme has been optimized for eddy identification based
179 on Liu et al. (2016). Firstly, the preliminary eddies filed is derived by a high pass filtering that
180 applied to global SLA data using a Gaussian filtering with a zonal/meridional radius of 10°/5°
181 before seed points (*i.e.*, the local SLA extrema point in closed contour). Secondly, the global
182 SLA fields are divided into 8×5 blocks with a zonal/meridional spacing of 45°/36°. Thirdly, SLA
183 contours are computed with a 0.25-cm interval, and eddy boundaries are subsequently extracted.
184 Finally, all blocks are merged seamlessly into a global map with duplicated eddies eliminated
185 (Chen and Han, 2019). This comprehensive eddy dataset is open access at
186 http://coadc.ouc.edu.cn/tfl/ or http://data.casearth.cn/ (Data ID: XDA19090202), the relevant
187 technical details and quality validation can be found in Liu et al. (2016). This data set has rich
188 parameters and multiple explicit eddy boundaries and the new version of 2019 has been
189 upgraded.

190 2.3 Hovmöller diagrams and 2D-FIR filter

191 The advantage of Hovmöller (or Time-longitude) diagrams is to exhibit the westward or
192 eastward propagation of the SLA signals in ocean fields by a static graph, that is, to show the
193 three-dimensional information in a 2D frame. the propagation patterns are evident in this
194 diagram, the left-upward tilt of a series continue values for westward, and the right-upward tilt
195 for eastward patterns. Meanwhile, the angle between this tilt and ordinate represents the
196 propagating speed. In the early stage, the main work was to evaluate the phase speed of oceanic
197 surface features by altimeter.

198 The 2D-FIR filter is an effective method, which can extract propagating wave-like
199 signals with a reference wave period and a first gauss phase speed in different basins first

proposed by Polito and Cornillon (1997) and then extended by Polito and Liu (2003). The small islands are ignored (zonal scale less than 3°) and only continuous open ocean (zonal scale more than 20°) areas are performed in this filter. The process includes three types of filter: a horizontally symmetric Gaussian-shaped filter is used to extract non-propagating signals and two slanted axially-symmetric Mexican-hat shaped filters are used to extract westward and eastward propagating signals. The zonal-temporal SLA fields are decomposed by a series of filters and followed these step:

$$Z_{ori} = Z_{t1} + Z_{24} + Z_{12} + Z_6 + (Z_{k6}) + Z_3 + (Z_{k3}) + Z_1 + (Z_{k1}) + Z_0 + (Z_{k0}) + Z_{t2} + Z_e + Z_r \quad (1)$$

Where Zori is the original SLA. The components are filtered in order and each one is removed from Zori before the next filter is applied. The components Zt1and Zt2 are obtained by applying a symmetric Gaussian filter, which targets non-propagating signals with annual or larger temporal scale. They are corresponding to filter spatial scale of an oceanic basin width and a 15° in zonal range, respectively. Components of Z24~Z3 are the anticipative westward propagating Rossby waves (may contain eddies) within centered periods of 24, 12, 6 and 3 months. The Z1 and Z0 components are attribute to the Tropical instability wave with period of 1.5 and 0.75 months, respectively. The Zk6~Zk0 are fast eastward propagating equatorial Kelvin waves and limited within latitude of ± 5.5°. The Ze is Mesoscale eddy signal that extracted by a symmetric Gaussian filter with 5° spatial and 50-day temporal window, which can include westward and eastward propagating eddies. The residual SLA variability Zr includes the mesoscale and small-scale features (or noise) that propagating speed different from Rossby waves.

The process of the filter applied from large to small scale in the order of formula (1), and a first gauss phase speed C_{p0} and reference period T (anticipative component period) are

required. According to the potential vorticity conservation of shallow water equation and the simplifying assumption of only zonal propagation of linear Rossby wave, one can lead to a relationship $C_{p0} \propto \frac{\cos(\theta)}{\sin(\theta)^2}$. The C_{p0} depends on the latitude θ and a poleward decrease in magnitude (Polito and Liu, 2003). Note that the final estimated phase speed C_p is obtained by a loop repeats until result converges to a stable value (*i.e.*, C_p change less than 10%), other parameters are also re-evaluated at the same time (*i.e.*, wavelength, amplitude).

3 Analyses the sampling capability of current satellite altimeters

Corresponding to the title, the well-known reason is under-sampling capability of altimeters in former research. In order to better demonstrate the great advance of on-orbit altimeters sampling capability, the three major phases of valid sampling capacity are contrasted in the region of 160°E~200°E, 25°N~45°N at Pacific and the result is shown in figure 1a. **1) Two satellite weekly product:** the gray lines are the Envisat and Jason-1 ground tracks during 17-Oct-2006 to 23-Oct-2006, these are corresponding to the merged altimetric product of a weekly resolution and a 0.25° grid that widely applied in oceanography research before the year of 2011. **2) Two satellite daily product:** the red lines are the ground tracks of Saral/Altika and Jason-3 satellites, they are re-occupying or succeeding the ERS and T/P mission, respectively. The main advantage of this version has a consistent error during all the period of time. **3) All satellite daily product:** the black lines are the ground tracks of Cryosat-2, HY-2A, OSTM/Jason-2 and Sentinel-3A satellites, and the red lines are the ground tracks of Saral/Altika and Jason-3 satellites in 20-Oct-2016. Contrasting with the three ground tracks, one can clearly find that the ground-track numbers of all satellite daily product are 3 times large than others and cross-track intervals are small than 10°.

To demonstrate the current sampling capability on mesoscale, we mark the detected mesoscale eddies effect boundaries (*i.e.,* the outermost enclosed contour of SLA surrounding the eddy centroid) by black contours under the satellite tracks in figure-1a. The color map corresponding to the preliminary eddies field, which derived by a Gaussian high-pass filter with zonal/meridional radius of 10°/5° (followed by Chelton et al., 2011a) from "all-sat" merged SLA. From figure 1a, the present altimetric product is insufficient to distinguish all adjacent mesoscale features caused by the inhomogeneous along-track sampling mode. Meanwhile, the track intervals are approximately the submesoscale under the dense sampling situation, such as the domain of 180E°~190°E in figure-1a. Combined with the advanced optimal interpolation algorithm, we believe that the coherent eddies hardly form too long scale wave-like patterns at the present.

Corresponding to the resolution of the merged SLA data, we also resampling the Level-3 along track observations within a grid of resolution in (1/4) °× (1/4) ° during 01-Aug-2016 to 30-Nov-2016, which have covered almost satellites revisit periods. In figure 1b, the latitudinal ground track intervals at daily averaged are compared with the mean radius of detected vortices during 2016 ~ 2019 (black line). The green, yellow, red and magenta lines are corresponding to the half of mean cross-track sampling interval that account for 70%, 80%, 90% and 100% of the census with different latitude, respectively (*e.g.,* 70% means removing the first and last 15% in the census data, others are similar). The Rossby radius of deformation (Rd) is marked by blue line and referred to Chelton et al. (1998), which defines the length scale of baroclinic variability longer than internal vortex stretching and the theoretical eddy scale is near 2.5~3 times of Rd. The relationship of spatial scale is only satisfied for latitude higher than 30° in figure 1b. Focus on these feature scales, one can find that the current on-orbit altimeters insufficient detect totally

mesoscale features in averaged scales. The mean radius of detected eddies is decrease from approximately 100 km in equator to 80 km in latitude of 60°. Accordingly, the half of mean cross-track sampling interval is decrease from 120 km to 30 km, respectively. In addition, the mean interval cannot reach 10 km which is the minimum order of mesoscale. Fortunately, the half of mean sampling interval can cover all mean eddies radius from the poleward of latitude 40° at the census statistics of 100% or latitude 25° at the census statistics of 70%. In other words, the current altimeter sampling capacity can distinguish coherent mesoscale eddies that out of the latitude of ±25° (likely) or ±40° (highly possible) statistically.

In addition, to further clarify the sampling capacity of the adjacent grid, we calculate the daily mean ratio of zero sampling interval (*i.e.*, two adjacent grids both have more than one sampling points) in 1/4°×1/4° resampling grid and marked by orange dash line in figure 1b. Through the statistics, we confirm that the directly and valid sampling of "all-sat" altimeters can distinguish more than 20% adjacent grids at equator and reach 55% at latitude of 60°. At this ratio, the problem of under-sampling remains serious and this is the biggest limitation of the contemporary satellite altimeter by a single point sampling mode. Moreover, the spatial resolution is near 7 km along the ground tracks and the unevenness of tracks distribution both can help for distinguish the coherent mesoscale or detect a fraction of submesoscale structures. It should note that submesoscale (≤10 km) features are not the content of this article, even they may directly affect altimeter observations within one grid.

Figure 1

4 Analyses the filtered components in Hovmöller diagrams

Mesoscale-eddies hardly form large-scale wave-like patterns in two-dimensional space, how about them in time-longitude diagram? An example of the filtered results is demonstrated in

figure 2 for 29.875°N at Pacific. Figure 2a is the original SLA and marked as Zori, and other panels in first row can constitute it. Zt (Zt1+Zt2) are non-propagating signals, Ze are mesoscale eddy signals and Zr are the residual signals, they have been explained in the above. Zw include all bottom panels wave-like components (Zw=Z24+Z12+Z6+Z3). Not other wave components are extracted because this latitude away from the equator. Firstly, one can compare the patterns of Zt and Zw component with Zori demonstrate the filter does not change the overall characteristics. Secondly, Ze are mainly shown as vortex signals with eastward propagation and anticipative Rossby wave components (Zw) contribute most of the westward propagating signals. Thirdly, Zr also includes some isolated and/or coherent eddy signals which temporal-spatial scale small than Ze signals. The last and most importantly, Z24~Z3 components are shown with homogeneous wave-like patterns and marked with evaluated wave parameters: Cp represents phase speed (negative for westward propagating), L represents wave length and Amp represents amplitude, the subscripts corresponding to periods of the components. From the estimated parameters, the wave length of Rossby waves from 2886 km at biannual periods decreased to 248 km at 3-month periods, the maximum amplitude is 61 mm at semiannual component and the largest phase speed is -4.85 km/day at annual component. The meridional band width (extreme value range) of wave components decrease from large periods to smaller periods, which corresponding to meridional spatial scale reasonably.

In addition, we also calculate the fractional variance (FV), which can quantify the proportion of each component in total. The similarity between Zori and Zs (Zs=Zori-Zr, *i.e.*, sum of all extracted components) is quantified by 98% FV of Zori explained by Zs. Every component is orthogonal, one can conclude that the filtering process did not add, extend or modify significantly these extrema (Polito and Sato, 2015). The detailed FV was shown in Table 1. From

all of comparison, we can find two point: 1) The discrepancy of meridional scale can be used as a criterion of the oceanic features in time-longitude diagram. 2) The proportion of ubiquitous mesoscale eddies is very small in original observed signals, the FV of Ze is only 3.68% and Ze+Zr is only 5.68%. It contradicts to the statistical fact that the identified eddies occupying ~43% of the oceanic area with no obvious polarity preference (Chen et al., 2020) and spontaneously leads to an idea: a patchwork of coherent eddies may pass through the filter that designed for extract Rossby wave signals.

Figure 2

Table 1

5 Mesoscale eddies masquerade as Rossby waves

5.1 The temporal-spatial scale

Aiming to demonstrate that filtered wave-like components may include detected mesoscale-eddies, we match eddy with filtered wave component. The identified eddy data sets have presented in section 2.2. There have been extensive studies of Rossby waves in the Indian Ocean (refer to section 1), and the latitude of 11.125°S is selected to show the matched results in figure 3. The filtered westward propagating SLA signals within the spectral band centered at 24, 12, 6 and 3 months of period in panels 3a~3d, respectively. Anticyclonic and cyclonic eddies (AEs and CEs) are marked as black and purple open circles, whose size is more than nine pixels in eddy identification. The circles' radius represents the observed meridional spatial scale.

Figure 3

Contrasting with the four panels in figure 3, it is clearly found that one eddy cannot form such wide band widths in Z24, Z12 and Z6 components and its diameter can approximately

correspond to the band width of Z3 components. As an evidence, wave length of the quarterly Rossby waves is 248 km in figure 2i, which is typical mesoscale. Moreover, eddies present an irregular distribution, both AEs and CEs exist on the crest or trough of the wave-like patterns. This figure mainly reflects the meridional scale difference between wave-like components and mesoscale eddies. In other words, mesoscale eddies hardly to masquerade as Rossby waves with period large than 6 months at present altimetric sampling density. One point should be noticed that the width of the bands is no gaps between one and its neighbors. The process of the filter guarantees that the bands are orthogonal among themselves by removing the part of correlated signals from the previously filtered bands.

5.2 The propagation speed

Taking the great advantage of the filtering algorithm for its availability of extracting the expected wave signals in individual oceanic basins and systematization of evaluating wave parameters with smaller statistical flections, the evaluate phase speed of wave-like patterns is compared with the speeds of nondispersive baroclinic Rossby waves predicted by classical linear theory. Figure 4 shows the estimated westward propagating speed of biannual and annual Rossby waves in 0.25° latitudinal resolution at three major basins and theory speed (refer to Chelton et al., 1998). In order to better show the local difference of the speeds, we discard the high values within near 10° of equator and other singular values (more than 20 cm/s). The propagation speed of nondispersive baroclinic Rossby waves is shown in figure 4 with black line, 2 times of theory speed is marked by the red dot line, and the red, green and blue sold circles in diagrams represent the speed derived from Pacific (a total of 97.30% and 91.67% in biannual and annual periods), Atlantic (a total of 97.60% and 95.52% in biannual and annual periods) and Indian Ocean (a total of 95.12% and 94.08% in biannual and annual periods) respectively. Firstly, the observed speeds

359 basically converge within 2 times of theory speed at two periods in both hemispheres. These
360 results basically consistent with Chelton and Schlax (1996), which have been attribute to
361 nonlinear mesoscale eddies in recently research (Chelton et al., 2007 and 2011a). Secondly, the
362 evaluate speed is compared in different basins. The speeds in Pacific are closer to theoretical
363 speeds than other basins. Atlantic and Indian Ocean appear below the theoretical speeds in mid-
364 latitude and more divergence than Pacific totally. Thirdly, the speed of two wave periods are
365 consistent patterns basically, especially in the southern hemisphere. Outside the latitude of ±25°,
366 the evaluated speeds begin to be significantly larger than theory values in the Atlantic and
367 southern hemisphere of the Indian Ocean. Beyond the latitude of 40°, the evaluated speeds
368 generally deviate from the standard theory. A possible interpretation of this propagation speed is
369 that SLA variability consists a superposition of nonlinear mesoscale eddies and larger-scale,
370 linear Rossby waves (Chelton et al., 2011a).

371 Figure 4

372 5.3 Wave-like patterns

373 Furthermore, the SLA of eddy fields are constructed in Hovmöller diagrams at Indian
374 Ocean 11.125°S and shown in figure 5. This figure directly demonstrates the fact that Rossby
375 waves and mesoscale-eddies are co-existence in altimetric products and filtered wave-like
376 components. Panel 5a is ZWE (ZWE=Zw+Ze), wave-like signals in 5b~5e are anticipative
377 Rossby waves, 5f~5g are the anticipative westward propagating Tropical Instability Waves with
378 central period of 1.5 and 0.75 months. Specially, the figure 5h is the SLA within detected eddies
379 and 5i is the SLA of preliminary eddies field that filtered by a spatially high-pass filter with a
380 zonal/meridional radius of 10°/5° (removed steric heating and cooling effects, as well as other
381 large-scale variability) from the original SLA product. The similar patterns can be found out by

382 comparing figure 5h and 5b~5g. On one hand, the SLA patterns of mesoscale eddies can be
383 traced significantly in filtered components with period of 3 and 1.5 months which are marked by
384 three black boxes (S1, S2, S3). On the other hand, the meridional scale of mesoscale eddies
385 cannot form the wave-like patterns of Z24 and Z12. In addition, as is shown in figure 5h and 5i,
386 the detected eddies signals contain the major patterns of filtered SLA and one remarkable
387 difference is that the coherent propagating signals in 5i becomes interrupted in 5h. One reason is
388 that eddy detected algorithm is based on spatial structure without consider time, and another
389 reason is eddies cannot maintain steady westward propagation. According to the statistics, nearly
390 8% for CE and 9% for AE are propagating purely zonally (Chelton et al., 2007). Thus, the long
391 wave-like patterns are rarely come from one vortex action and mainly attribute to the adjacent
392 eddies in time-longitude diagram. A noticeable example in figure 5i is that the non-large scale
393 signals can form a wave-like pattern with period more than 1 year, but the meridional scale is
394 limited at mesoscale. These adjacent eddies transport with similar speed as Rossby wave,
395 therefore forming wave-like patterns and masquerade as long planetary Rossby wave in
396 Hovmöller diagrams. This figure explains why eddies can pass through the special 2D-FIR filters
397 that intended to avoid them in earlier studies.

398 Figure 5

399 Moreover, corresponding to the components of figure 5, the FV of each component is
400 shown in Table 2 and the correlation of the detected eddies and filtered wave-like components is
401 shown in Table 3. The correlation also supported that mesoscale eddies hardly masquerade as
402 Rossby waves patterns with period large than 6 months at present altimetric sampling density in
403 this latitude. The highest correlation is more than 60% in Z1.5 and second is near 24% in Z3 and
404 Z0.75 components. The FV and correlation between detected eddies (figure 5h) and Zori and

405 preliminary eddy signals (figure 5i) are calculated. The results reveal that detected eddies explain
406 16.30% of original signals and 67.40% of preliminary eddy signals, and correlations are 50.84%
407 and 82.04%, respectively. However, Amores et al. (2018) concluded that gridded products
408 capture only between 6% and 16% of the total number of eddies. The main reason is a huge
409 number of submesoscale eddies cannot be captured by contemporary altimeters. Also, the
410 unresolved structures are aliased into larger structures in the gridded products.

411 Table 2

412 Table 3

413 In order to confirm the above arguments, the 2D-FIR filter is applied to SLA signals in
414 figure 5i again and the results are shown in figure 6. Delightfully, this filter only decomposed out
415 the wave-like components of Z6~Z0.75 and the westward propagating patterns in figure 6b~6e
416 are similar to the counterparts in figure 5d~5g. Therefore, we reveal that the special 2D-FIR filter
417 can successfully extract the wave-like patterns in Hovmöller diagrams. However, the diagram
418 essentially demonstrates 3-dimensional information in a form of 2-dimension and the theoretical
419 independent topological relationship of eddies in spatial domain becomes tightly coherent
420 patterns in temporal-spatial domain. So, these anticipative wave-like patterns also include real
421 Rossby wave signals and spurious wave signals that masqueraded by eddies.

422 Figure 6

423 5.4 Analysis the fake waves

424 The cross-track sampling interval of current satellite altimeter has been analyzed in
425 section 3, but these sampling intervals may also result in an error of fake waves. Thus, aiming to
426 support the reliability of the filter results, we introduce three well-know intrinsic characteristics
427 of altimeter sampling and propose three arguments: 1) the sampling intervals decrease from

equator to poleward regularly. In other words, the ratio of wave-like signals by the aliasing of the sampling interval and oceanic mesoscale features will decrease with latitude increase. 2) the sampling is symmetry in both hemispheres which means the ratio of wave-like signals will approximately symmetry. 3) the fake wave patterns will betray themselves at dense sampling domain, such as the high latitude and dense cross-track domain (*e.g.*, 180°E~190°E in figure 1a). The latitudinal FV of the biannual and annual components is shown in figure 7 and the latitudinal variation of the half of mean sampling interval (same as 100% census in figure 1b) is also marked on it. By contrasting the variation trend, one can significantly find that the variational trends are inverse and hemispheric asymmetry, which can help us to eliminate the mainly concern of the sampling mechanism.

Figure 7

6 Quantify the oceanic Rossby waves signals

It is confirmed that the decomposed wave-like components include Rossby waves and vortices signals. However, the magnitude of Rossby wave signals in the oceans is still unknown. Based on the problem, we try to quantify the ratio of eddy masqueraded signals and the real Rossby wave signals at present data.

Based on all of the above argumentations, the latitudinal variations of oceanic Rossby waves with central periods of 24, 12 and 6 months at critical latitude of linear theory prediction (The latitude $\leq 45°$, Challenor et al., 2001) are quantified. The critical latitude depends on the frequency, while higher frequencies confined closer to the Equator, and poleward of which no propagation is possible (Mysak, 1983). In addition, outside the equatorial region the phase speed of the Rossby waves are indicative of the first baroclinic mode and inside the equatorial region shows that a relatively weak component can be contaminated by fast waves (Polito and Liu,

2003). The region of 10°S~10°N has large spatial sampling interval and Rossby radius of deformation, and more complex fluctuation phenomena (Such, tropical instability wave, kelvin wave *et al.*). However, there are few number of detected eddies and picturesquely called as "eddy deserts" by Chen and Han (2019). So, the statistics also exclude the equatorial areas within ±10°.

Final statistics are based on the difference between the filtered wave components of original SLA and preliminary eddies fields, and the results are shown in figure 8. The panels 8a~8c correspond to the latitudinal variations of fractional variance in Pacific with centered wave periods of 24, 12 and 6 months. Panels 8d~8f are in Atlantic and Panels 8g~8i are in Indian Ocean, respectively. The blue (red) lines represent the ratio of anticipative (real) Rossby waves, and the black dot lines represent the ratio of masquerade waves.

Figure 8

As a whole, the dominant wave signals are generally observed for biannual and annual Rossby waves, while semiannual Rossby waves are weakest. This conclusion is slightly different with former conclusion that the annual periods are the dominant wave signals (Polito and Liu, 2003), and the reason is the elimination of wave-like signals that mainly masquerade by mesoscale eddies. Moreover, the three basins also have their own characteristics. The Pacific is the widest ocean basin which is the center stage of ENSO. Thus, there are most significant biannual and annual Rossby wave signals. Simultaneously, the fractional variance of semiannual Rossby wave in there is also higher than other counterpart, with maximum more than 10% at equatorward of 20°S. Meanwhile, the linear Rossby waves riding on the zonal mean flow regard dominant teleconnection patterns that gain energy from the zonally varying background flow (Simmons et al., 1983; Xie et al., 2016). There are the significant enhancement of eddy and wave

signals outside 35°N, which may relate to modulation of the Kuroshio currents and its extension. In Atlantic, the ratio of the Rossby waves signals is lower on the whole, but it is satisfied the rule that the fractional variance is decrease with period. There is a Gulf Stream enhancement effect outside of 30°N. In Indian Ocean, the clearest and most energetic wave signals are annual Rossby waves. It is also teleconnection with ENSO, which phase-locked to the annual cycle and the last act of ENSO drama is played over the Indo-western Pacific after the curtain falls on the main stage (Xie et al., 2016).

A noticeable point that the ratio of spurious waves decreases with latitude increase. In other words, eddies can masquerade as Rossby wave only within a limited latitude (the ratio is 0). The limited latitude also supports or confirms the well-known idea that most of the propagating energy near tropics in the form of Rossby waves rather than eddies (*e.g.*, Chelton et al., 2007). Firstly, the intrinsic reason is the under-sampling temporal-spatial resolution of altimeters that has been analyzed in section 3. Meanwhile, the limited latitude is directly related to the oceanic basin (contrast with figure-8a,8d and 8g) and the local characteristics of eddy (such as the regions of western boundary currents have greater eddy density). In addition, the differences of limited latitude are also reflected in periods of masqueraded waves. An example of the Pacific, the limited latitude is near poleward of 25°S and 20°N in biannual period component, and poleward of 10°S and 10°N in annual period component. While in semiannual period the limited latitude is inside the 10°S and 10°N. Other factors, such as the background current and bottom topography, may also affect the limited latitude.

7 Summary and Concluding Remarks

Two decades ago, oceanic Rossby waves were first evaluated by satellite altimeter from sea level signals. However, they were identified as nonlinear mesoscale eddies in a decade later.

The nonlinear eddies can masquerade as wave-like patterns and the problem perpetuate in former researches. As a result, the oceanic Rossby waves are not definitely extracted from altimetric products. Using the five or six satellites altimeters merged SLA products during 2016~2019 and the specially 2D-FIR filters, the Rossby waves and eddies are re-investigated and the ratio of first baroclinic Rossby waves in three major basins are quantified independently, yielding the following main results:

First, the sampling density of "all-sat" merged products are analyzed. The newly product has more than 3 times of sampling density than former products. However, the maximum interval is close to 10° in mid-latitude and hardly to distinguish all the adjacent mesoscale features since the insufficient and inhomogeneous of the along-tracks sampling. In addition, the ratio of adjacent grids with one or more sampling points is larger than 20% in equator and reach the highest value of 55% in latitude of 60°. Statistically, the current altimeter sampling capability can distinguish mesoscale eddies out of the latitude of ±25° (likely) or ±40° (highly possible).

Second, a series of 2D-FIR filters are applied in newly altimetric products and the results strictly demonstrate that adjacent eddies can masquerade as long planetary Rossby waves in Hovmöller diagrams and pass through the filter. Therefore, the theoretical independent topological relationship of eddies in spatial domain becomes tightly coherent patterns in temporal-spatial domain.

Third, the ratios of masquerade wave and the real Rossby wave signals in observed SLA are quantified. The dominant wave signals are generally observed for biannual and annual Rossby waves that the maximum appears in mid-latitude Pacific with more than 25% of observed signals and only more than 15% in Atlantic and Indian Ocean. While semiannual Rossby waves are weak, with lower than 5% in Atlantic especially. The Pacific is the main stage

of ENSO and ratio of Rossby waves is larger than other basins significantly. Meanwhile, the most energetic wave signals are annual Rossby waves in Indian Ocean, which can be attributed to ENSO of the phase-locked to the annual cycle.

In conclusion, mesoscale eddies can still masquerade as Rossby wave in newly merged altimetric products and the authoritative 2D-FIR filters fail to distinguished them directly. The ratio of masquerade wave signals and real Rossby wave signals is quantified by involving the preliminary eddies field. A limited latitude that eddies can masquerade as Rossby waves should be noticed, and it also confirm or reveal that the most of propagating energy near tropics in the form of Rossby waves rather than eddies. Further researches are needed to explore the dynamic formations behind these multi-spectral bands of the Rossby waves and the physical process of coupling mechanism between waves and vortices, and assess its role in energy cascade and dynamic balance that contribute to the study of global climate change.

Acknowledgments

This research was jointly supported by the National Natural Science Foundation of China (Grant No. 42030406), the Qingdao National Laboratory for Marine Science and Technology of China (Grant No. 2018SDKJ102), and the Ministry of Science and Technology of China (Grant No. 2016YFC1401008). We are grateful to Dr. Paulo S. Polito (Universidade de São Paulo) for the algorithms of 2D FIR filter. The altimeter all-sat merged sea level anomaly (SLA) data used in this study are distributed by Copernicus Marine Environment Monitoring Service (CMEMS; https://marine.copernicus.eu/). Edited altimeter eddy data is available at http:/data.casearth.cn/ (Data ID: XDA19090202) through Tian et al. (2019).

References

Barron, C. N., Kara, A. B., & Jacobs, G. A. (2009). Objective estimates of westward Rossby wave and eddy propagation from sea surface height analyses. *Journal of Geophysical Research: Oceans*, *114*(C3).

Birol, F., & Morrow, R. (2001). Source of the baroclinic waves in the southeast Indian Ocean. *Journal of Geophysical Research: Oceans*, *106(C5)*, 9145-9160.

Bosc, C., & Delcroix, T. (2008). Observed equatorial Rossby waves and ENSO-related warm water volume changes in the equatorial Pacific Ocean. *Journal of Geophysical Research: Oceans*, *113*(C6).

Challenor, P. G., Cipollini, P., & Cromwell, D. (2001). Use of the 3D Radon transform to examine the properties of oceanic Rossby waves. *Journal of Atmospheric and Oceanic Technology*, *18*(9), 1558-1566.

Chambers, D. P., Tapley, B. D., & Stewart, R. H. (1999). Anomalous warming in the Indian Ocean coincident with El Nino. *Journal of Geophysical Research: Oceans*, *104*(C2), 3035-3047.

Charria, G., Dadou, I., Cipollini, P., Drévillon, M., De Mey, P., & Garçon, V. (2006). Understanding the influence of Rossby waves on surface chlorophyll concentrations in the North Atlantic Ocean. *Journal of marine research*, *64*(1), 43-71.

Chelton, D. B., DeSzoeke, R. A., Schlax, M. G., El Naggar, K., & Siwertz, N. (1998). Geographical variability of the first baroclinic Rossby radius of deformation. *Journal of Physical Oceanography*, *28*(3), 433-460.

Chelton, D. B., & Schlax, M. G. (1996). Global observations of oceanic Rossby waves. *Science*, *272*(5259), 234-238.

564 Chelton, D. B., & Schlax, M. G. (2003). The accuracies of smoothed sea surface height fields
565 constructed from tandem satellite altimeter datasets. *Journal of Atmospheric and Oceanic*
566 *Technology, 20(9)*, 1276-1302.

567 Chelton, D. B., Schlax, M. G., Samelson, R. M., & de Szoeke, R. A. (2007). Global observations
568 of large oceanic eddies. *Geophysical Research Letters, 34*(15).

569 Chelton, D. B., Schlax, M. G., & Samelson, R. M. (2011a). Global observations of nonlinear
570 mesoscale eddies. *Progress in oceanography*, *91*(2), 167-216.

571 Chelton, D. B., Gaube, P., Schlax, M. G., Early, J. J., & Samelson, R. M. (2011b). The influence
572 of nonlinear mesoscale eddies on near-surface oceanic chlorophyll. *Science*, *334*(6054), 328-332.

573 Chen, G., & Han, G. (2019). Contrasting short-lived with long-lived mesoscale eddies in the
574 global ocean. *Journal of Geophysical Research: Oceans*, *124*(5), 3149-3167.

575 Chen, G., Chen, X., & Huang, B. (2020). Independent eddy identification with profiling Argo as
576 calibrated by altimetry. *Journal of Geophysical Research: Oceans*, e2020JC016729.

577 Chowdary, J. S., Gnanaseelan, C., & Xie, S. P. (2009). Westward propagation of barrier layer
578 formation in the 2006–07 Rossby wave event over the tropical southwest Indian Ocean.
579 *Geophysical Research Letters*, *36*(4).

580 Chu, P. C., Ivanov, L. M., Melnichenko, O. V., & Wells, N. C. (2007). On long baroclinic
581 Rossby waves in the tropical North Atlantic observed from profiling floats. *Journal of*
582 *Geophysical Research: Oceans*, *112*(C5).

583 Cipollini, P., Cromwell, D., Challenor, P. G., & Raffaglio, S. (2001). Rossby waves detected in
584 global ocean colour data. *Geophysical Research Letters, 28(2)*, 323-326.

585 Cipollini, P., Cromwell, D., Jones, M. S., Quartly, G. D., & Challenor, P. G. (1997). Concurrent
586 altimeter and infrared observations of Rossby wave propagation near 34 N in the Northeast
587 Atlantic. *Geophysical Research Letters*, *24(8)*, 889-892.

588 Cipollini, P., Quartly, G. D., Challenor, P. G., Cromwell, D., & Robinson, I. S. (2006). Remote
589 sensing of extra-equatorial planetary waves. *American Society for Photogrammetry and Remote*
590 *Sensing*.

591 Dickinson, R. E. (1978). Rossby waves--long-period oscillations of oceans and atmospheres.
592 *Annual Review of Fluid Mechanics*, *10*(1), 159-195.

593 Gill, A. E., *Atmosphere-Ocean Dynamics*, *Int. Geophys. Ser.*, Vol. 30, 662 pp., Academic, San
594 Diego, Calif., 1982.

595 Gutknecht, E., Dadou, I., Charria, G., Cipollini, P., & Garcon, V. (2010). Spatial and temporal
596 variability of the remotely sensed chlorophyll a signal associated with Rossby waves in the South
597 Atlantic Ocean. *Journal of Geophysical Research: Oceans*, *115*(C5).

598 Hill, K. L., Robinson, I. S., & Cipollini, P. (2000). Propagation characteristics of extratropical
599 planetary waves observed in the ATSR global sea surface temperature record. *Journal of*
600 *Geophysical Research: Oceans*, *105(C9)*, 21927-21945.

601 Killworth, P. D., Chelton, D. B., & de Szoeke, R. A. (1997). The speed of observed and
602 theoretical long extratropical planetary waves. *Journal of Physical Oceanography*, *27*(9), 1946-
603 1966.

604 Killworth, P. D., & Blundell, J. R. (1999). The effect of bottom topography on the speed of long
605 extratropical planetary waves. *Journal of physical oceanography*, *29(10)*, 2689-2710.

606 Killworth, P. D., & Blundell, J. R. (2003a). Long extratropical planetary wave propagation in the
607 presence of slowly varying mean flow and bottom topography. Part I: The local problem.
608 *Journal of Physical Oceanography*, *33*(4), 784-801.

609 Killworth, P. D., & Blundell, J. R. (2003b). Long extratropical planetary wave propagation in the
610 presence of slowly varying mean flow and bottom topography. Part II: Ray propagation and
611 comparison with observations. *Journal of physical oceanography*, *33*(4), 802-821.

612 Killworth, P. D. (2004). Comment on" Oceanic Rossby Waves Acting As a 'Hay Rake' for
613 Ecosystem Floating By-Products". *Science*, *304(5669)*, 390-390.

614 Killworth, P. D., Cipollini, P., Uz, B. M., & Blundell, J. R. (2004). Physical and biological
615 mechanisms for planetary waves observed in satellite-derived chlorophyll. *Journal of*
616 *Geophysical Research: Oceans*, *109*(C7).

617 Liu, Y., Chen, G., Sun, M., Liu, S., & Tian, F. (2016). A parallel SLA-based algorithm for global
618 mesoscale eddy identification. *Journal of Atmospheric and Oceanic Technology*, *33*(12), 2743-
619 2754.

620 Masumoto, Y., & Meyers, G. (1998). Forced Rossby waves in the southern tropical Indian
621 Ocean. *Journal of Geophysical Research: Oceans*, *103*(C12), 27589-27602.

622 McGillicuddy, D. J. (2011). Eddies masquerade as planetary waves. *Science*, *334*(6054), 318-
623 319.

624 Mysak, L. A. (1983). Generation of annual Rossby waves in the North Pacific. *Journal of*
625 *physical oceanography*, *13*(10), 1908-1923.

626 O'Brien, R. C., Cipollini, P., & Blundell, J. R. (2013). Manifestation of oceanic Rossby waves in
627 long-term multiparametric satellite datasets. *Remote sensing of environment*, *129*, 111-121.

628 Pedlosky, J., *Geophysical Fluid Dynamics*, 2nd ed., Springer-Verlag, New York, 1986.

629 Perigaud, C., & Delecluse, P. (1993). Interannual sea level variations in the tropical Indian
630 Ocean from Geosat and shallow water simulations. *Journal of Physical Oceanography*, *23(9)*,
631 1916-1934.

632 Polito, P. S., & Cornillon, P. (1997). Long baroclinic Rossby waves detected by
633 TOPEX/POSEIDON. *Journal of Geophysical Research: Oceans*, *102*(C2), 3215-3235.

634 Polito, P. S., & Liu, W. T. (2003). Global characterization of Rossby waves at several spectral
635 bands. *Journal of Geophysical Research: Oceans*, *108*(C1).

636 Polito, P. S., & Sato, O. T. (2015). Do eddies ride on Rossby waves? *Journal of Geophysical*
637 *Research: Oceans*, *120*(8), 5417-5435.

638 Polito, P. S., Sato, O. T., & Liu, W. T. (2000). Characterization and validation of the heat storage
639 variability from TOPEX/Poseidon at four oceanographic sites. *Journal of Geophysical Research:*
640 *Oceans*, *105*(C7), 16911-16921.

641 Quartly, G. D., Cipollini, P., Cromwell, D., & Challenor, P. G. (2003). Rossby waves: Synergy
642 in action. *Philosophical Transactions of the Royal Society of London. Series A: Mathematical,*
643 *Physical and Engineering Sciences*, *361*(1802), 57-63.

644 Simmons, A. J., Wallace, J., & Branstator, G. W. (1983). Barotropic wave propagation and
645 instability, and atmospheric teleconnection patterns. *Journal of the Atmospheric Sciences*, *40*(6),
646 1363-1392.

647 Uz, B. M., Yoder, J. A., & Osychny, V. (2001). Pumping of nutrients to ocean surface waters by
648 the action of propagating planetary waves. *Nature*, *409(6820)*, 597-600.

649 Xie, S. P., Annamalai, H., Schott, F. A., & McCreary Jr, J. P. (2002). Structure and mechanisms
650 of South Indian Ocean climate variability. *Journal of Climate*, *15*(8), 864-878.

651 Xie, S. P., Kosaka, Y., Du, Y., Hu, K., Chowdary, J. S., & Huang, G. (2016). Indo-western
652 Pacific Ocean capacitor and coherent climate anomalies in post-ENSO summer: A review.
653 *Advances in Atmospheric Sciences*, *33*(4), 411-432.

654

655

656

657

658

659

660

661

662

663

664

665

666

667

668

669 **Table**

670

671 **Table 1.** Fractional Variance Explained by Each Component of the SLA Data

Components	Zori	Zs	Zr	Zt	Zw	Ze	Z24	Z12	Z6	Z3
$\%\sigma^2$	100.00	98.00	2.00	26.10	68.35	3.68	17.91	15.40	26.73	8.31

672

673 **Table 2.** Fractional Variance Explained by Each Component of the SLA Data

Comp.	Zori	Zs	Zr	Zt	Ze	Z24	Z12	Z6	Z3	Z1	Z0
$\%\sigma^2$	100.00	98.65	1.35	26.22	3.46	11.45	24.00	6.43	8.86	15.31	2.06

674

675 **Table 3.** The correlation between the detected eddies and filtered westward propagating
676 components in figure 4.

Comp.	Z24	Z12	Z6	Z3	Z1.5	Z0.75	ZE
%corr.	1.88	11.34	10.73	24.06	61.84	24.81	16.80

677

678

679

680

681

682

683

684

685

686

687

688

Figure Captions

Figure 1. The sampling capacity of the on-orbit altimeters: (a) Color map scale in centimeter shows SLA of the preliminary eddies filed (high-pass filtering with a zonal/meridional radius of 10°/5° on original SLA) in 20-Oct-2016. Effect boundaries of the identified eddies are marked by black contours, which corresponding to the color map. Eddies core is marked as a plus sign. The black lines represent the ground tracks of Cryosat-2, HY-2A, OSTM/Jason-2 and Sentinel-3A satellites and red lines represent the ground tracks of Saral/Altika Drifting Phase and Jason-3 satellites. The gray lines represent the ground tracks of Envisat and Jason-1 in 17-Oct-2006 to 23-Oct-2006. (b) Latitudinal variations of the sampling interval and feature census. The black line represents the mean radius of the mesoscale eddies in 2016-2019 and the blue line represents the Rossby radius of deformation. The green, yellow, red and magenta lines represent the half mean sampling interval of on-orbit altimeters during 01-Aug-2016 to 30-Nov-2016, which corresponding to 70%, 80%, 90% and 100% of all census, respectively. The orange dash line represents the ratio of zero interval in resampled grid.

Figure 2. The Hovmöller diagrams of decomposed SLA at 29.875°N in the Pacific: (a) Zori: original AVISO data; (b) Zt: sum of all large-scale, nonpropagating signal; (c) Zw: sum of all wave-like components; (d) Ze: mesoscale residuals mainly eastward propagation; (e) Zr: small scale residual; (f)~(i) Z24 to Z3: westward propagating signals with 24~3 months of period, and the basin-average phase speed (cp), wavelength (L) and amplitude (Amp) also marked in the corresponding components. Color map scale in millimeter.

711 Figure 3. Similar to figure 2 for Indian Ocean 11.125°S. The mesoscale eddies overlay on
712 Z24, Z12, Z6 and Z3 components. The black and purple open circles represent AE and CE which
713 size more than nine pixels in eddy identification and eddy core at 11.125°S. The radius
714 represents the observed meridional spatial scale.
715
716 Figure 4. The latitudinal variation of the westward propagation speeds of filtered
717 evaluation and the standard theory of nondispersive baroclinic Rossby waves. The waves with
718 central period of 24 months in (a) and 12 months in (b). The red, green and blue sold circles in
719 diagrams represent the Pacific, Atlantic and Indian Ocean, respectively. The propagation speed
720 of nondispersive baroclinic Rossby waves is shown by the black line and 2 times of theory speed
721 is shown by the red dot line.
722
723 Figure 5. Similar to figure 2 for Indian Ocean 11.125°S. Panel (a): ZWE show the sum of
724 anticipated westward waves and mesoscale eddies components. Panel (h): the SLA within
725 detected eddies. Three black boxes (S1, S2, S3) indicate the SLA patterns of mesoscale eddies
726 can be traced in filtered components with period of 3 and 1.5 months remarkably. Panel (i): the
727 preliminary eddies field and marked by filtered SLA.
728
729 Figure 6. Similar to figure 2 for Indian Ocean 11.125°S. The 2D FIR filters were applied
730 in panel (a) and decomposed panels (b)~(f).
731
732 Figure 7. Latitudinal variation of the filtered biannual and annual wave-like components
733 and half of sampling interval.

Figure 8. Latitudinal variation of the Rossby wave components with biannual, annual and semiannual period at three basins. The blue lines corresponding to the filtered wave-like components of original SLA, the black dot lines corresponding to the masquerade wave components and red lines corresponding to the real wave components.

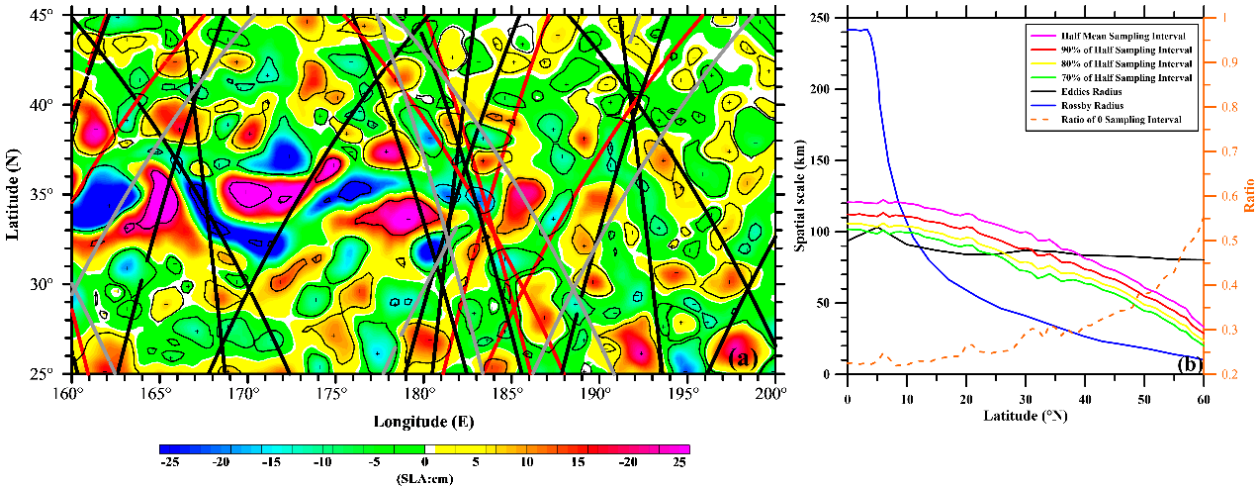

Figure 1. The sampling capacity of the on-orbit altimeters: (a) Color map scale in centimeter shows SLA of the preliminary eddies filed (high-pass filtering with a zonal/meridional radius of 10°/5° on original SLA) in 20-Oct-2016. Effect boundaries of the identified eddies are marked by black contours, which corresponding to the color map. Eddies core is marked as a plus sign. The black lines represent the ground tracks of Cryosat-2, HY-2A, OSTM/Jason-2 and Sentinel-3A satellites and red lines represent the ground tracks of Saral/Altika Drifting Phase and Jason-3 satellites. The gray lines represent the ground tracks of Envisat and Jason-1 in 17-Oct-2006 to 23-Oct-2006. (b) Latitudinal variations of the sampling interval and feature census. The black line represents the mean radius of the mesoscale eddies in 2016-2019 and the blue line represents the Rossby radius of deformation. The green, yellow, red and magenta lines represent the half mean sampling interval of on-orbit altimeters during 01-Aug-2016 to 30-Nov-2016, which corresponding to 70%, 80%, 90% and 100% of all census, respectively. The orange dash line represents the ratio of zero interval in resampled grid.

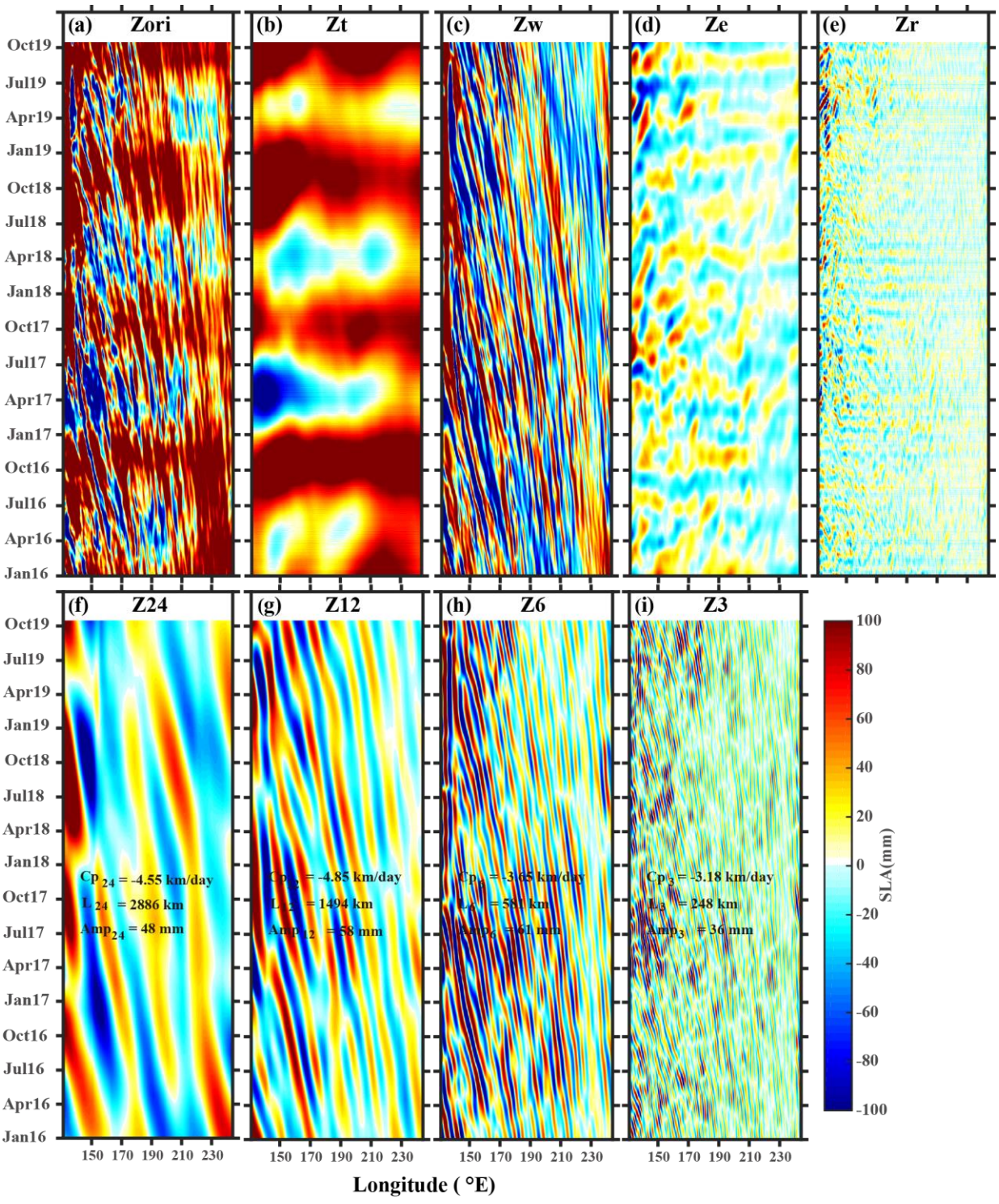

Figure 2. The Hovmöller diagrams of decomposed SLA at 29.875°N in the Pacific: (a) Zori: original AVISO data; (b) Zt: sum of all large-scale, nonpropagating signal; (c) Zw: sum of all wave-like components; (d) Ze: mesoscale residuals mainly eastward propagation; (e) Zr:

small scale residual; (f)~(i) Z24 to Z3: westward propagating signals with 24~3 months of period, and the basin-average phase speed (cp), wavelength (L) and amplitude (Amp) also marked in the corresponding components. Color map scale in millimeter.

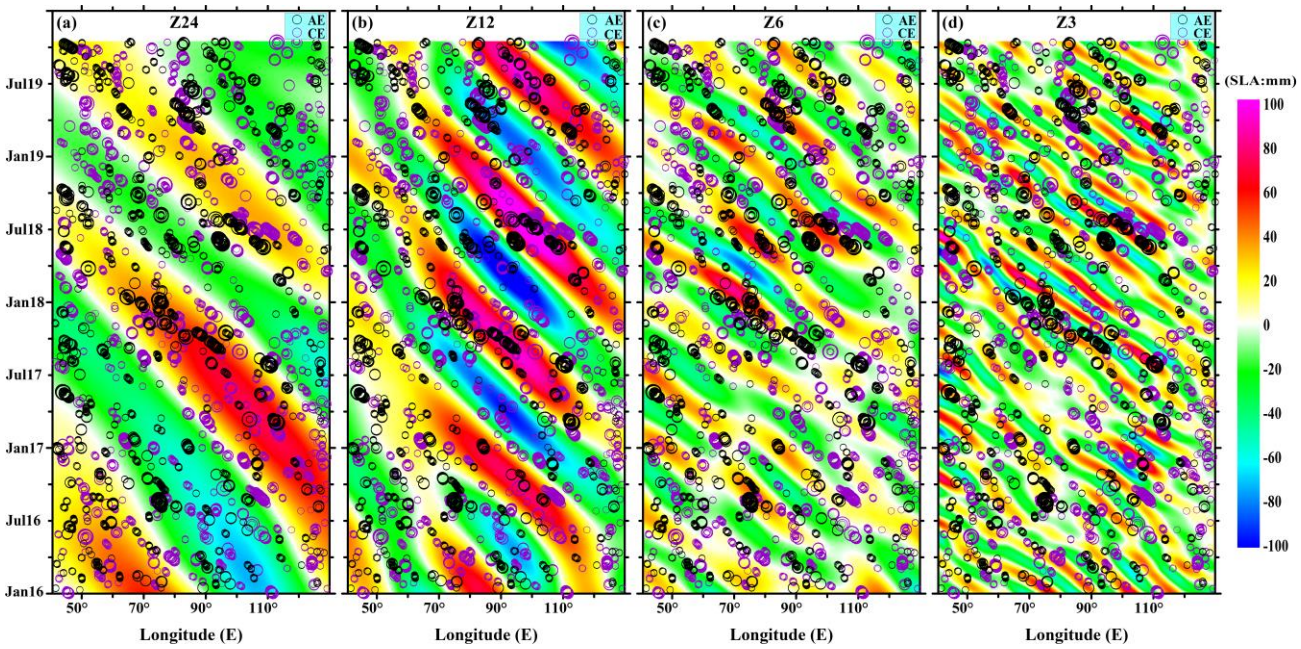

Figure 3. Similar to figure 2 for Indian Ocean 11.125°S. The mesoscale eddies overlay on Z24, Z12, Z6 and Z3 components. The black and purple open circles represent AE and CE which size more than nine pixels in eddy identification and eddy core at 11.125°S. The radius represents the observed meridional spatial scale.

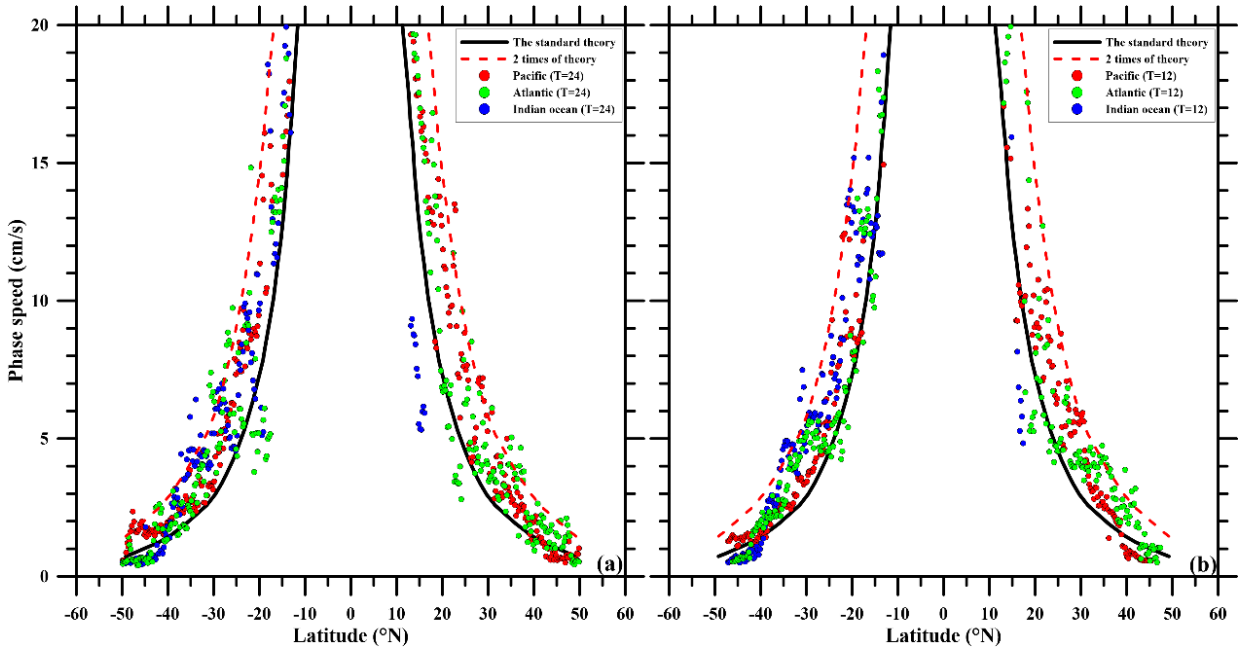

Figure 4. The latitudinal variation of the westward propagation speeds of filtered evaluation and the standard theory of nondispersive baroclinic Rossby waves. The waves with central period of 24 months in (a) and 12 months in (b). The red, green and blue sold circles in diagrams represent the Pacific, Atlantic and Indian Ocean, respectively. The propagation speed of nondispersive baroclinic Rossby waves is shown by the black line and 2 times of theory speed is shown by the red dot line.

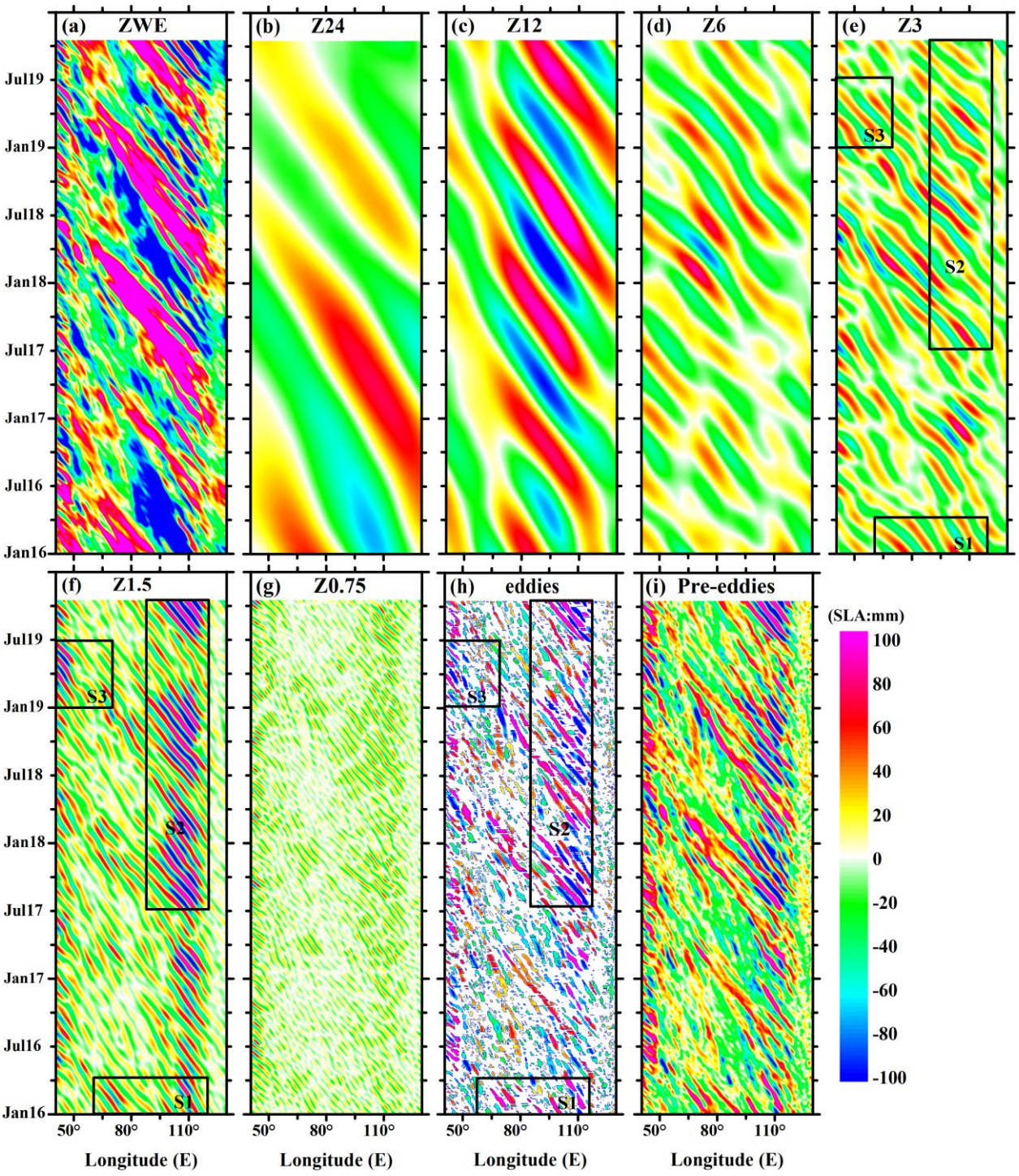

Figure 5. Similar to figure 2 for Indian Ocean 11.125°S. Panel (a): ZWE show the sum of anticipated westward waves and mesoscale eddies components. Panel (h): the SLA within detected eddies. Three black boxes (S1, S2, S3) indicate the SLA patterns of mesoscale eddies

can be traced in filtered components with period of 3 and 1.5 months remarkably. Panel (i): the preliminary eddies field and marked by filtered SLA.

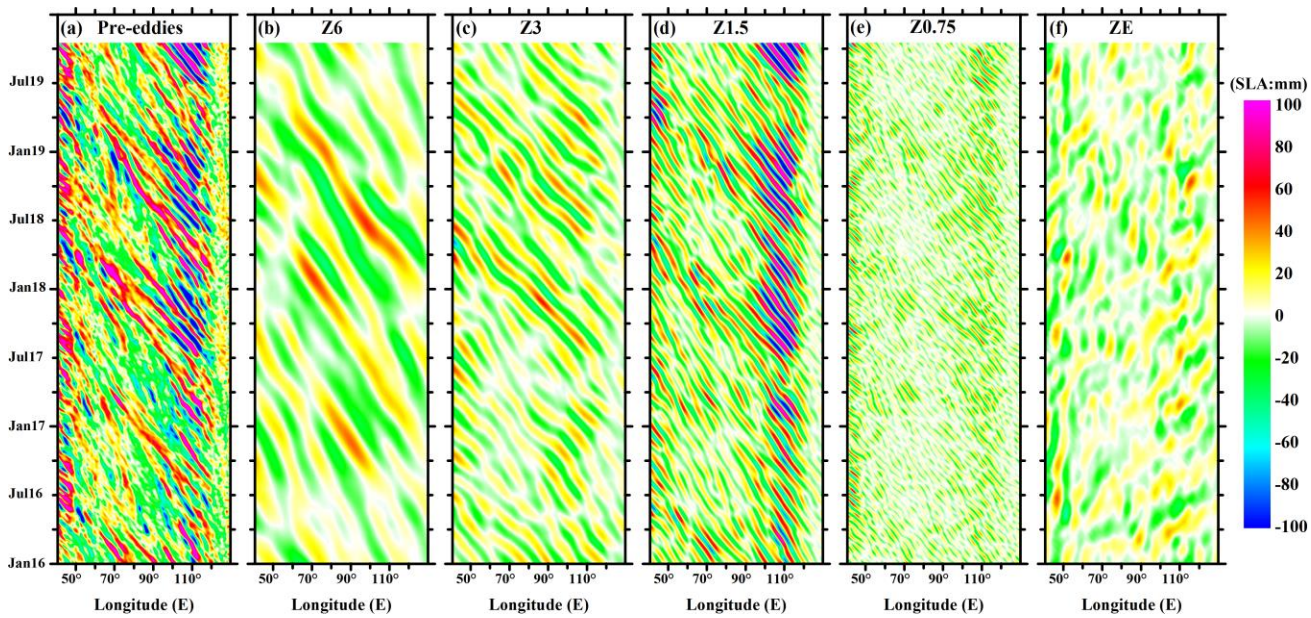

Figure 6. Similar to figure 2 for Indian Ocean 11.125°S. The 2D FIR filters are applied in panel (a) and decomposed panels (b)~(f).

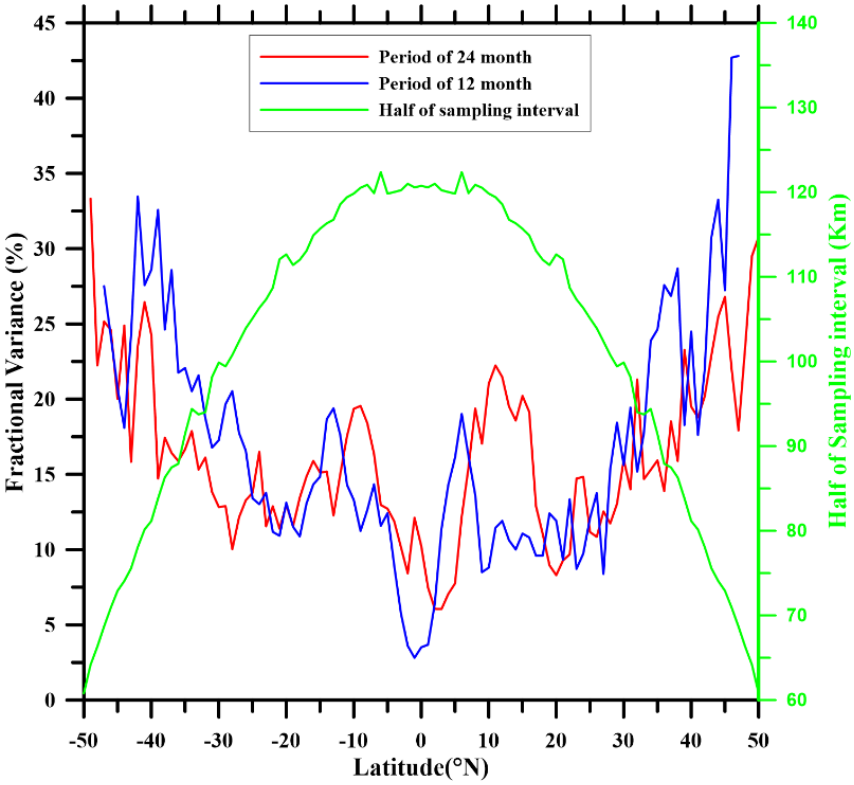

Figure 7. Latitudinal variation of the filtered biannual and annual wave-like components and half of sampling interval.

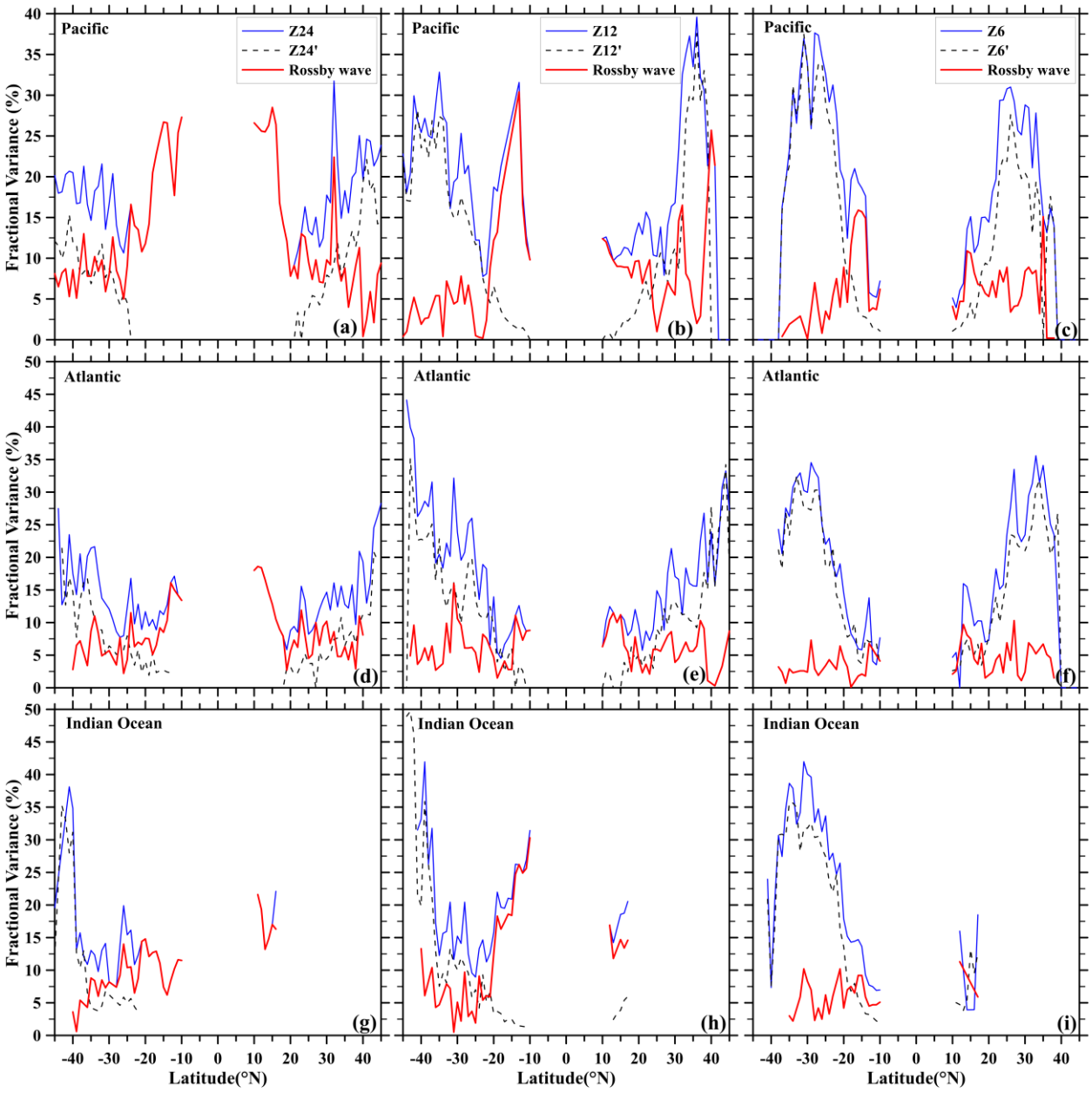

Figure 8. Latitudinal variation of the Rossby wave components with biannual, annual and semiannual period at three basins. The blue lines corresponding to the filtered wave-like components of original SLA, the black dot lines corresponding to the masquerade wave components and red lines corresponding to the real wave components.